Scorodite precipitation in the presence of antimony

David Kossoff [a], Mark D. Welch [b], Karen A. Hudson-Edwards [a,*]

[a] Department of Earth and Planetary Sciences, Birkbeck, University of London, Malet St., London WC1E 7HX, UK
[b] Department of Earth Science, The Natural History Museum, Cromwell Road, London SW7 5BD, UK

ARTICLE INFO

ABSTRACT

The effects of Sb on the precipitation of synthetic scorodite, and the resultant phases formed, were investigated. Nine synthetic precipitates with varying concentrations of Sb, together with As-only and Sb-only end members, were prepared using a scorodite synthesis method, and these were characterised using XRD, SEM, chemical digestion and μXRF mapping. XRD analysis shows that the end members are scorodite ($FeAsO_4 \cdot 2H_2O$) and tripuhyite ($FeSbO_4$), and that the intermediate members are not Sb-substituted scorodite, but instead are physical mixtures of scorodite and tripuhyite, with tripuhyite becoming more prominent with increasing amounts of Sb in the synthesis. Electron microprobe analysis on natural scorodites confirms that they contain negligible concentrations of Sb. With increasing Sb in the synthesis, the morphology of the scorodite changes from rosettes of intergrown crystals to anhedral masses of smaller crystallites. Chemical digestion of the series also became increasingly difficult with increasing Sb content. We conclude that Sb is not taken up in scorodite (perhaps due to its larger ionic radius and different co-ordination with O compared to As), that increasing amounts of Sb in the system affect scorodite morphology, and that tripuhyite is a highly stable and perhaps underestimated Sb-sink.

1. Introduction

Arsenic (As) and antimony (Sb) are classified as priority pollutants in the United States and European Union (Filella et al., 2002) because ingestion of As- and Sb-bearing fluids or inhalation of As- and Sb-bearing particles can lead to pathologies such as cardiovascular disease and lung cancer (Pershagen et al., 1987; Centeno et al., 2002; Yáñez et al., 2003; States et al., 2011; Maiti et al., 2012). One of the major sources of As and Sb in the environment is mine wastes, which contain 10s to 10,000s of ppm of As and 10s to 1000s of ppm of Sb (Smedley and Kinniburgh, 2002; Wu et al., 2011; Cidu et al., 2014). There has been a near exponential increase in the physical amount of waste rock extracted by modern mining principally as a function of the increasing use of opencast methods (Mudd, 2010). This volume of waste is predicted to grow over the next 100 years due to increasing demand for mineral resources, and with the consequent exploitation of ever-lower ore grades (Gordon et al., 2006). Therefore, the amount of mine waste-derived As and Sb will correspondingly increase. Though precise numbers of people directly affected by mine waste-derived Sb are not available, they are likely to be in the range of 10s to 100s of thousands, given that 10,000 inhabitants are impacted in the Sb mining area of Xikuangshan, China alone (Fu et al., 2010). Large numbers of people are also affected by mining-related As contamination throughout the world. For example, in the former tin mining area of Ron Phibun (Thailand) 1000 people were found to be directly affected by arsenicosis, with 30,000 more at risk.

One of the ways that the risks posed by exposure to As and Sb can be mitigated is by the precipitation of minerals and especially, those that are relatively insoluble and have resultingly low bioaccessibility. The two principal primary sources of As in mine tailings are arsenopyrite, with 46 wt.% As, and (arsenical) pyrite, with up to ~3 wt.% As (e.g., Savage et al., 2000; Kossoff et al., 2012). These minerals are hosts for Sb (Friedl et al., 1992) with, for example, <0.001–0.143 wt.% Sb (mean 0.34 wt.%) in arsenopyrite and <0.0002–0.039 wt.% Sb (mean 0.012 wt.%) in pyrite (Kossoff et al., 2012). The major primary host of Sb in mine wastes is stibnite (Sb_2S_3) (e.g., Kossoff et al., 2012; Roper et al., 2012). These primary As and Sb minerals frequently occur together (e.g., Wilson et al., 2004; Anawar et al., 2011), and it is therefore likely that their secondary (alteration) phases will also be associated.

One of the major secondary As-bearing phases in mine wastes is scorodite, which has been shown to have the lowest bioaccessibility of common As-bearing mine waste minerals at pH values > 4 (Salzsauler et al., 2005; Meunier et al., 2010; Nordstrom et al., 2014). Scorodite is considered to be a stable phase, particularly under oxic conditions (Drahota and Filippi, 2009), but under reducing conditions (Eh < 100 mV) it is destabilized, often as a result of the activity of organisms such as Fe(III)-reducing bacteria (Cummings et al., 1999). Although Sb is known to be present in mining-affected environments where scorodite occurs (e.g., Haffert and Craw, 2008), its potential effects on scorodite precipitation and character, and the resultant Sb phases formed, are

* Corresponding author. Tel.: +44 203 073 8030.
E-mail address: k.hudson-edwards@bbk.ac.uk (K.A. Hudson-Edwards).

not well-known. To fill this knowledge gap, we conducted co-precipitation experiments with Sb and scorodite, and we examined natural scorodite samples for the presence of Sb. This study therefore aimed to determine how the presence of Sb affects scorodite precipitation, and to characterise the solid phases produced.

2. Methods and materials

2.1. Synthetic Fe–As–Sb–O compounds

2.1.1. Synthesis methods

The method of Paktunc et al. (2008) was used to synthesise scorodite-type compounds with zero to 100 M Sb/(As + Sb). The method was modified by carrying out the synthesis in sealed reaction bombs with PTFE liners, rather than on a hotplate. The bombs were set in a 140 ± 3 °C oven for three days (72 h). Eleven precipitates containing various proportions of As and Sb were synthesised (Table 1). The syntheses were carried out using 0.1 M HCl solution (pH 1) and 0.2 M sodium arsenate heptahydrate ($Na_2HAsO_4 \cdot 7H_2O$) and sodium antimonate trihydrate ($Na_3SbO_4 \cdot 3H_2O$), depending on the relative amounts of As and Sb desired in the precipitates (Table 1), and 0.1 M ferric sulphate ($Fe_2(SO_4)_3 \cdot 5H_2O$) pentahydrate (equivalent to 0.2 M $Fe(SO_4)_{1.5} \cdot 5H_2O$).

2.1.2. Characterisation of synthetic precipitates

The precipitates were photographed using a Nikon D300S camera and their colours were recorded using a Munsell colour chart. The precipitates were then identified by X-ray powder diffraction using a PANalytical XPERT-PRO diffractometer (45 kV, 40 mA) with CuKα radiation monochromated by a Ge(111) plate. Anti-scatter Soller slits were used and the precipitates were spun at 0.5 rev s^{-1}. A constant step-scan interval of 0.0167° was used from 10 to 80 °2θ corresponding to 4189 data points. Total exposure times of 5 h were used to obtain patterns for Rietveld refinement of precipitates $As_{100}Sb_0$, $As_{98.75}Sb_{1.25}$, $As_{95}Sb_5$, $As_{90}Sb_{10}$, $As_{60}Sb_{40}$ and $As_{50}Sb_{50}$, comprising mixtures of well-crystallised scorodite (with or without minor poorly crystallised tripuhyite). An exposure time of 3 h was used for those precipitates containing poorly crystallised tripuhyite that were unsuitable for Rietveld refinement, but allowed peaks to be identified and indexed. The detection limit of the diffractometer based upon scorodite: tripuhyite ratio (by mass) was estimated by preparing mixtures of precipitates $As_{100}Sb_0$ (pure scorodite) and As_0Sb_{100} (pure tripuhyite). It was found that scorodite peaks could be detected and peak positions determined at the 2 wt.% level, which we take to be a good indication of the phase detection limit for our diffraction experiments.

The morphology and size of the precipitates were analysed using scanning electron microscopy (SEM, JEOL JSM-6480LV) following Au coating. For the imaging secondary electrons were collected using a 7 kV acceleration voltage. The relative proportions of As, Sb, Fe and O in the synthetic precipitates were determined by Wavelength-dispersive X-ray spectroscopic (WDS) analysis (EMPA; Jeol 8100 Superprobe) on polished resin blocks. Analyses were carried out using an accelerating voltage of 15 kV, a current of 2.5 nA and a beam diameter of 1 μm. The counting times for all elements were 20 s on the peak, and 10 s each on the high and low backgrounds. The analyses were calibrated against standards of natural silicates, oxides and Specpure® metals, with the data corrected using a ZAF program (Gill, 1997).

For quantitative total element analysis, approximately 200 mg of the synthetic precipitates were dissolved in a PTFE beaker by adding 10 mL of concentrated HNO_3. This digestion methodology proved difficult, however, for the more Sb-rich members of the series. The concentrated HNO_3 digestion was successful only with precipitates $As_{100}Sb_0$, $As_{98.75}Sb_{1.25}$, $As_{95}Sb_5$, $As_{90}Sb_{10}$ and $As_{60}Sb_{40}$; for the remaining precipitates the HNO_3 was evaporated, 5 mL HF and a further 2 mL of concentrated HNO_3 were added, and the mixture was then complexed with 1 mL perchloric acid ($HClO_4$) and evaporated. Subsequently, 5 mL of concentrated HNO_3 was added and the solution was made up to 100 mL with 18 MΩ cm^{-1} deionised water to give a 5% (vol:vol) HNO_3 matrix suitable for inductively coupled plasma atomic emission spectroscopy (ICP-AES) analysis. This additional procedure successfully digested precipitates $As_{50}Sb_{50}$, $As_{40}Sb_{60}$ and $As_{10}Sb_{90}$, but portions of precipitates As_5Sb_{95}, $As_{1.25}Sb_{98.75}$ and As_0Sb_{100} increasingly remained as milky-coloured precipitates. A heated ultrasonic bath was employed over a period of 6 h in a final attempt to dissolve these precipitates.

2.2. Collection and electron microprobe analysis of natural scorodite and tripuhyite samples

Natural samples of scorodite (n = 36) were obtained from museum collections at Birkbeck College (London, UK), the Natural History Museum (London, UK), the Manchester Museum (Manchester, UK), the Smithsonian Institution (Washington DC, USA), the Victoria Museum (Melbourne, Australia), the American Museum of Natural History (New York, New York, USA) and the Natural History Museum (Salt Lake City, Utah, USA) and from mineral dealers. The samples were photographed using a Nikon D300S camera and their relative proportions of As, Sb, Fe and O were determined by electron microprobe analysis using the same instrument as described above.

2.3. μXRF analysis of synthetic precipitates

To investigate the distribution and association of As and Sb in the synthetic precipitates, we carried out micro-X-ray fluorescence (μXRF) mapping at the Sb L^{III} and As K edges at the Diamond Light Source on beamline I18 on polished blocks previously analysed by EPMA. Operating conditions for the storage ring were 3 GeV and 200 mA. On I18, which is an undulator beamline, the X-rays are focused by a pair of Kirkpatrick–Baez (KB) mirrors after being monochromated by a Si(111) double-crystal monochromator. Harmonic rejection for Sb was achieved by reflecting off the silicon substrate of the KB mirrors. The beam size for the μXRF was 5 μm.

Table 1
Details of synthesis of As–Sb–Fe–O compounds.

Precipitate	$Fe_2(SO_4)_3 \cdot 5H_2O$ (mg)	$Na_2HAsO_4 \cdot 7H_2O$ (mg)	$Na_2SbO_4 \cdot 3H_2O$ (mg)	As (mol/L)	Sb (mol/L)	As/(As + Sb) molar	Sb/(As + Sb) molar
$As_{100}Sb_0$	0.490	0.624	0.000	0.2000	0.0000	100	0
$As_{98.75}Sb_{1.25}$	0.490	0.609	0.012	0.1975	0.0025	98.75	1.25
$As_{95}Sb_5$	0.490	0.593	0.025	0.1950	0.0050	95	5
$As_{90}Sb_{10}$	0.490	0.562	0.049	0.1900	0.0100	90	10
$As_{60}Sb_{40}$	0.490	0.374	0.197	0.1200	0.0800	60	40
$As_{50}Sb_{50}$	0.490	0.312	0.247	0.1000	0.1000	50	50
$As_{40}Sb_{60}$	0.490	0.250	0.296	0.0800	0.1200	40	60
$As_{10}Sb_{90}$	0.490	0.063	0.444	0.0100	0.1900	10	90
As_5Sb_{95}	0.490	0.031	0.469	0.0050	0.1950	5	95
$As_{1.25}Sb_{98.75}$	0.490	0.016	0.487	0.0025	0.1975	1.25	98.75
As_0Sb_{100}	0.490	0.000	0.490	0.0000	0.2000	0	100

3. Results and discussion

3.1. Characterisation of synthetic precipitates

The different combinations of $Fe_2(SO_4)_3 \cdot 5H_2O$, $Na_2HAsO_4 \cdot 7H_2O$ and $Na_3SbO_4 \cdot 3H_2O$ (Table 1) produced pale green (Munsell colour 7.5GY 8/1) and orange-red precipitates (Munsell colour 5YR 6/8) (Fig. 1). Precipitate $As_{100}Sb_0$ was pure pale green, whereas precipitate As_0Sb_{100} was pure orange-red. A small number of orange-red crystals was present within precipitate $As_{98.75}Sb_{1.25}$, and the relative abundance of these crystals increased in precipitates $As_{95}Sb_5$ and $As_{90}Sb_{10}$. Precipitates $As_{60}Sb_{40}$, $As_{50}Sb_{50}$, $As_{40}Sb_{60}$, $As_{10}Sb_{90}$ and $As_{1.25}Sb_{98.75}$ became increasingly orange-red and homogeneous in colour as the amount of Sb in the precipitates increased (Fig. 1).

3.1.1. XRD

Powder XRD patterns of all precipitates are shown in Fig. 2. Examples of Rietveld refinements for precipitates $As_{100}Sb_0$ and $As_{60}Sb_{40}$ are shown in Fig. 3, and an enlargement of the diffraction pattern of As_0Sb_{100} is shown in Fig. 4. The numerical results of Rietveld refinements are summarised in Table 2, and unit-cell parameters as a function of composition are plotted in Fig. 5.

Powder diffraction patterns of $As_{100}Sb_0$, $As_{98.75}Sb_{1.25}$, $As_{95}Sb_5$ and $As_{90}Sb_{10}$ indicate single-phase scorodite as the only crystalline precipitate. No impurity peaks were observed. As the Sb content of the starting material increases (precipitates $As_{60}Sb_{40}$, $As_{50}Sb_{50}$, $As_{40}Sb_{60}$ and $As_{10}Sb_{90}$), four new very broad peaks located at approximately 27.0 °2θ (d_{hkl} ~ 3.30 Å), 35.0 °2θ (d_{hkl} ~ 2.56 Å), 53.3 °2θ (d_{hkl} ~ 1.72 Å) and 67.5 °2θ (d_{hkl} ~ 1.39 Å) appear and grow, being superimposed upon the scorodite patterns (Figs. 2 and 3). These peaks are assigned to poorly crystallised tripuhyite and correspond to {110}, {011}, {121} and {031}, respectively. Nonetheless, it was possible to refine meaningful unit-cell parameters for scorodite from the two-phase patterns of $As_{60}Sb_{40}$ and $As_{50}Sb_{50}$ (Table 2). For $As_{40}Sb_{60}$ and $As_{10}Sb_{90}$ the
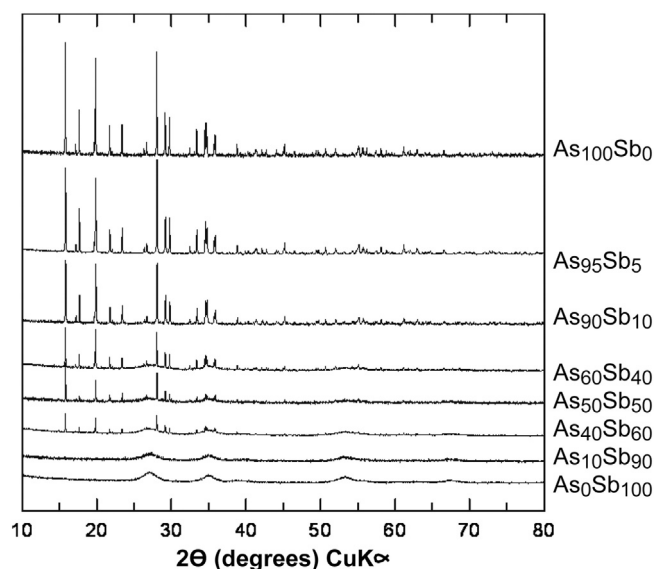
Fig. 2. XRD patterns for precipitates $As_{100}Sb_0$, $As_{95}Sb_5$, $As_{90}Sb_{10}$, $As_{60}Sb_{40}$, $As_{50}Sb_{50}$, $As_{40}Sb_{60}$, $As_{10}Sb_{90}$ and As_0Sb_{100}.

interference from broad tripuhyite peaks was too severe to refine meaningful cell parameters. However, by eye, the positions of scorodite peaks (which remain sharp) in diffraction patterns of these precipitates are very similar to those of more As-rich compositions for which cell parameters were derived. Precipitates from more Sb-rich starting compositions gave diffraction patterns containing only the four broad tripuhyite peaks.

Rietveld refinement was carried out using *GSAS* (Larson and Von Dreele, 2004). The following global variables were refined to convergence initially before then refining structural variables: scale
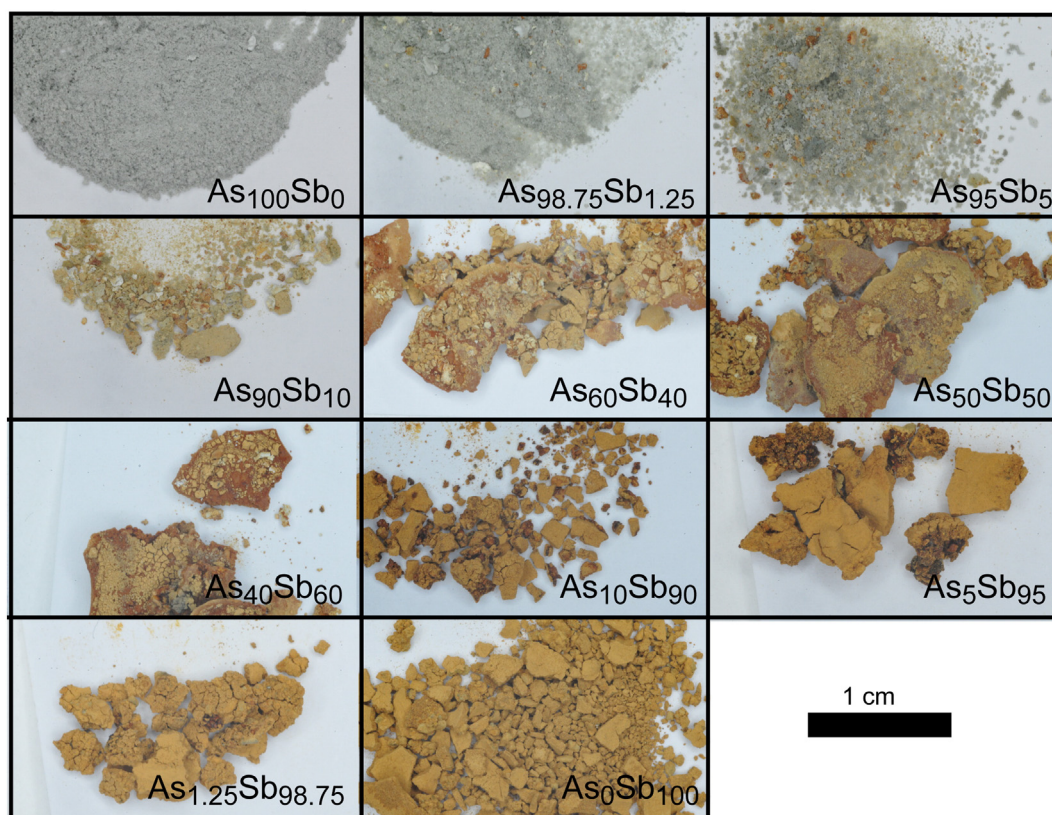

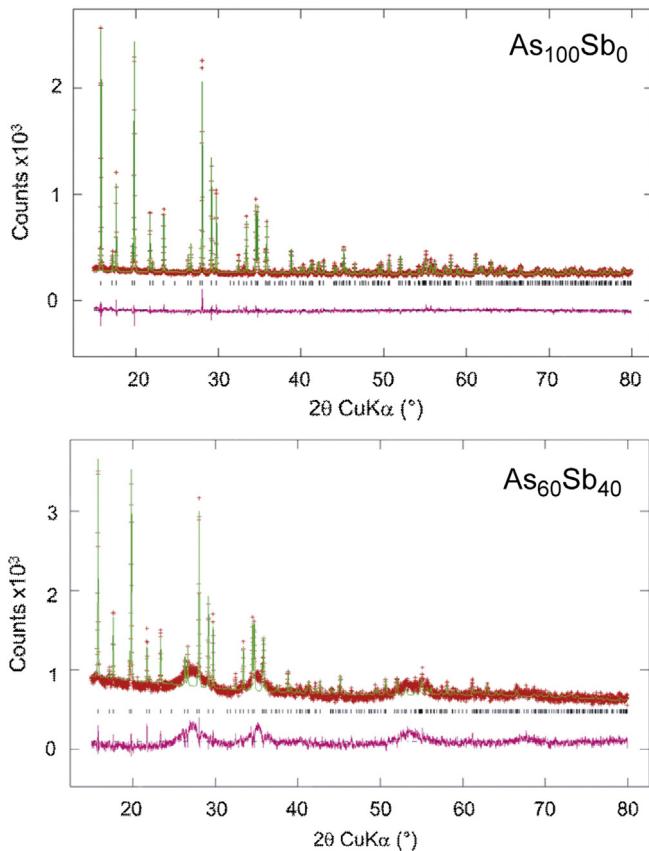**Fig. 1.** Photographs of synthetic precipitates.

Fig. 3. Detailed Rietveld refinements of precipitates $As_{100}Sb_0$ and $As_{60}Sb_{40}$.

Table 2
Unit cell parameters from Rietveld fitting. One-sigma values are shown in brackets.

Sample	a (Å)	b (Å)	c (Å)	V (Å³)	Rp	wRp
$As_{100}Sb_0$[a]	8.9515(2)	10.0456(2)	10.3220(2)	928.18(4)	0.051	0.064
$As_{100}Sb_0$[b]	8.9517(3)	10.0454(3)	10.3219(3)	928.19(6)	0.050	0.063
$As_{98.75}Sb_{1.25}$	8.9528(2)	10.0465(2)	10.3216(2)	928.37(5)	0.036	0.053
$As_{95}Sb_5$	8.9536(2)	10.0469(2)	10.3192(2)	928.28(5)	0.026	0.036
$As_{90}Sb_{10}$	8.9531(4)	10.0443(4)	10.3212(4)	928.16(8)	0.042	0.053
$As_{60}Sb_{40}$	8.9510(7)	10.0459(7)	10.3208(8)	928.1(2)	0.056	0.072
$As_{50}Sb_{50}$	8.9503(9)	10.0451(8)	10.3195(9)	927.8(2)	0.062	0.082

[a] 1 h scan.
[b] 5 h scan.

(several very broad but minor peaks), it proved possible to refine meaningful and well-constrained unit-cell parameters for scorodite. The starting model for all refinements was the structure of scorodite reported by Xu et al. (2007) in orthorhombic space group *Pbca*. Note that this setting of the orthorhombic cell is related to the alternative *Pcab* setting sometimes reported for scorodite (e.g., Majzlan et al., 2012) by the transformation matrix [001/100/010] for *Pbca* → *Pcab*. The series of refinements began with precipitate $As_{100}Sb_0$ (pure scorodite) and the resulting model used as the basis for refinements of precipitates $As_{98.75}Sb_{1.25}$, $As_{95}Sb_5$, $As_{90}Sb_{10}$, $As_{60}Sb_{40}$ and $As_{50}Sb_{50}$.

Scorodite unit-cell parameters are essentially invariant within two standard uncertainties for all precipitates in which it is present (Table 2, Fig. 2), and are in close agreement (when transformed) with the corresponding values reported for synthetic scorodite by Majzlan et al. (2007), e.g., for 200/Majzlan: $a = 8.9517/8.9512$ Å, $b = 10.0454/10.0438$ Å, $c = 10.3219/10.3247$ Å, and are also similar to those for synthetic scorodite compounds collected previously (e.g., Savage et al., 2005; Jia et al., 2006; Paktunc et al., 2008; Paktunc and Bruggeman, 2010). There is no clear evidence for scorodite in precipitate $As_{10}Sb_{90}$, suggesting either that it was below the detection limit of the XRD instrument (2 wt.%) or that there is some As incorporated in the tripuhyite. The peaks for tripuhyite are significantly more diffuse than those for scorodite. This is likely a function of the comparatively disordered relationship between Fe and Sb in the former phase. Indeed, some authors have claimed that there is no long-range order between Sb and Fe (Berlepsch et al., 2003). However, Grau-Crespo et al. (2004) modelled a Fe/Sb ordering along the long (c) axis of the tetragonal cell, while detecting no interaction along either a (or b) axis. Hence, the diffraction patterns of tripuhyite might be predicted to be more diffuse than those of scorodite as a function of this comparative disorder, together with the former's commonly reported nano-sized crystal habit (e.g., Mitsunobu et al., 2011; Lalinská-Voleková et al., 2012).

3.1.2. SEM

The crystal system of scorodite is reported to be orthorhombic–dipyramidal (Recio-Vazquez et al., 2011). This is shown clearly in $As_{100}Sb_0$, $As_{98.75}Sb_{1.25}$, $As_{95}Sb_5$ and $As_{90}Sb_{10}$ (Fig. 6), in which the precipitates are rosettes of intergrown crystals, similar to those previously reported for synthetic abiotic and biotic scorodite (Gonzalez-Contreras et al., 2010; Majzlan et al., 2012, respectively). The crystals in $As_{100}Sb_0$ range in size from c. 2 to 40 μm (average 30 μm), those in $As_{98.75}Sb_{1.25}$ range in size from c. 1 to 30 μm (average 20 μm), while those in $As_{95}Sb_5$ range in size from c. 1 to 40 μm (average 15 μm). The morphology of the series changed as a function of the increasing Sb/As ratio, becoming increasingly blocky as the series ascended, with the most significant change occurring between precipitates $As_{90}Sb_{10}$ and $As_{60}Sb_{40}$. Precipitates $As_{60}Sb_{40}$, $As_{50}Sb_{50}$, $As_{40}Sb_{60}$, $As_{10}Sb_{90}$, As_5Sb_{95} and $As_{1.25}Sb_{98.75}$ resemble those of Le Berre et al. (2008), who synthesised poorly crystalline material (obtained through spontaneous precipitation) which was highly aggregated (around 60 μm in size) consisting of nanocrystallites (pH 2, 80 °C, 6–9 h crystallisation time).

factor, zero-point, 3–6 background parameters (a cosine-Fourier series), profile parameters (U, V, W and LX) and unit-cell parameters. Atom coordinates and isotropic displacement parameters were determined for all atoms. In order to stabilise refinements to convergence, it was necessary to refine shared U_{iso} for all four non-H_2O oxygen atoms and also tie together U_{iso} of the oxygen atoms of the two independent H_2O molecules. For the refinements of the patterns of $As_{60}Sb_{40}$ and $As_{50}Sb_{50}$, both of which contain a significant tripuhyite component, it was necessary to omit refinement of atom coordinates and all U_{iso}(fixed at 0.02 Å²). As we are primarily interested only in deriving unit-cell parameters from Rietveld refinements, these limitations did not have any deleterious effect upon the quality of cell parameters.

Despite the presence of a poorly crystallised tripuhyite component in the diffraction patterns of precipitates $As_{60}Sb_{40}$ and $As_{50}Sb_{50}$

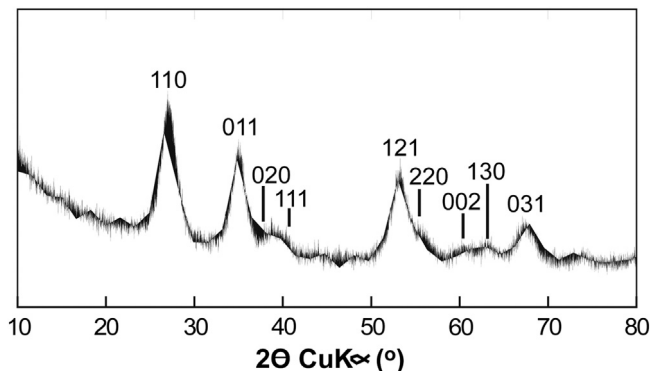

Fig. 4. Enlargement of XRD pattern for precipitate As_0Sb_{100} (tripuhyite) showing main peaks and their associated d-spacings.
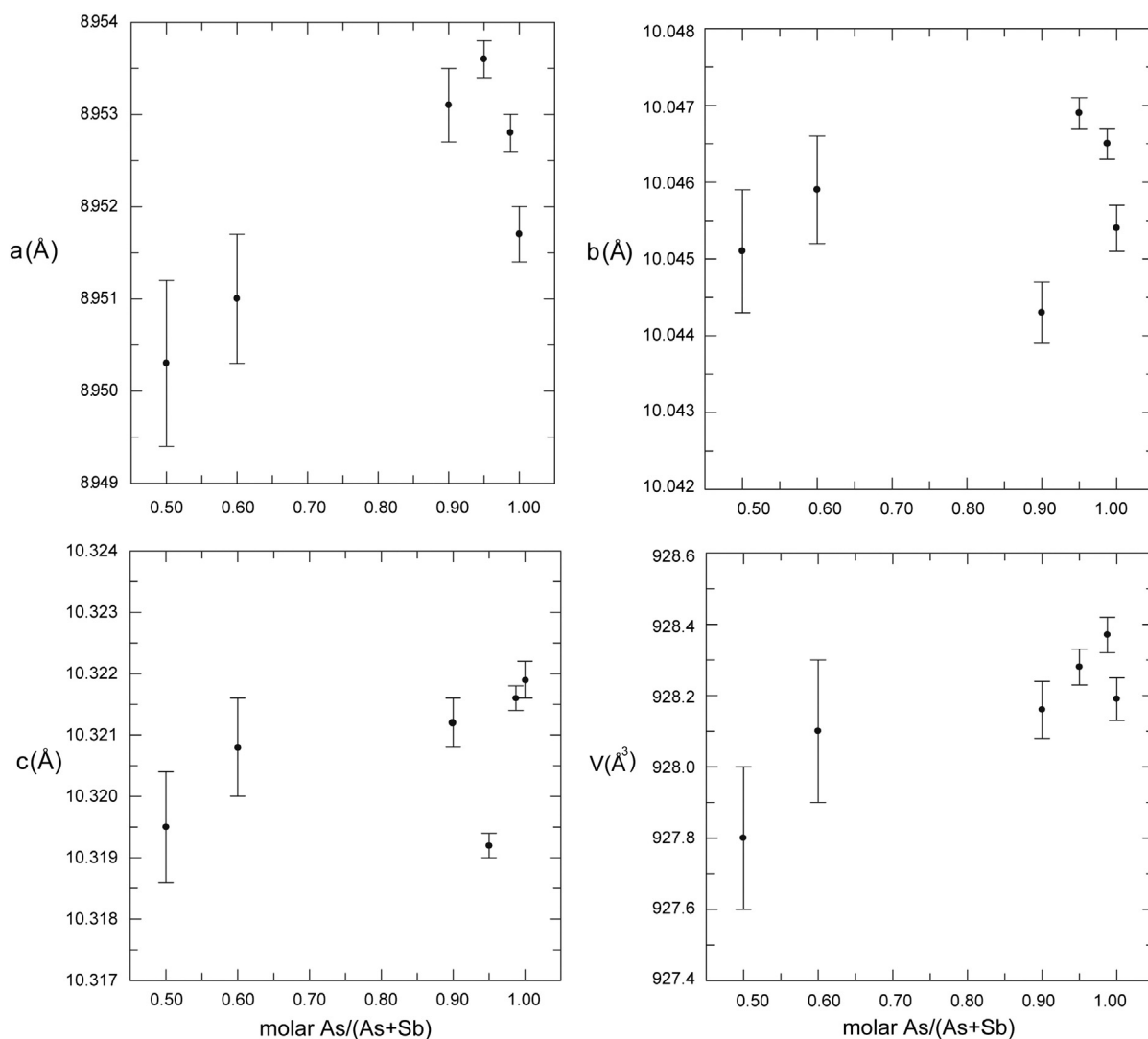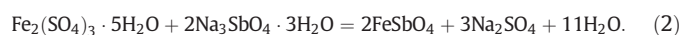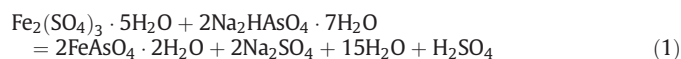
Fig. 5. Scorodite unit cell parameter X–Y plots.

The crystal system of tripuhyite is reported as tetragonal (Berlepsch et al., 2003). Crystallites in the tripuhyite precipitate As_0Sb_{100} and in precipitate $As_{1.25}Sb_{98.75}$ exhibit such morphologies, with grains sizes ranging from c. 0.25 to 10 μm (average 3 μm) in $As_{1.25}Sb_{98.75}$ and from c. 0.25 to 30 μm (average 5 μm) in As_0Sb_{100}. The top parts of these ranges are comparable to those previously reported for tripuhyite (~100 × 300 μm, Fig. 7b in Majzlan et al., 2011), although, as with other authors, Majzlan et al. (2011) report nano-scale domains for this mineral.

Electron microprobe analysis of 47 synthetic scorodite grains in $As_{100}Sb_0$ and $As_{98.75}Sb_{1.25}$, and of 103 synthetic tripuhyite grains in $As_{1.25}Sb_{98.75}$ and As_0Sb_{100} give Fe:As and Fe:Sb atomic % ratios of 51 ± 1:49 ± 1 and 45 ± 5:55 ± 5, respectively, which are in range of ideal scorodite and tripuhyite, at 50:50 each.

3.1.3. Chemical digestions

The yields for the precipitates were calculated by assuming that precipitates $As_{100}Sb_0$ and As_0Sb_{100} formed in scorodite and tripuhyite as written the following equations:

$$Fe_2(SO_4)_3 \cdot 5H_2O + 2Na_2HAsO_4 \cdot 7H_2O$$
$$= 2FeAsO_4 \cdot 2H_2O + 2Na_2SO_4 + 15H_2O + H_2SO_4 \qquad (1)$$

$$Fe_2(SO_4)_3 \cdot 5H_2O + 2Na_3SbO_4 \cdot 3H_2O = 2FeSbO_4 + 3Na_2SO_4 + 11H_2O. \qquad (2)$$

For the intermediate members of the synthetic series it was assumed that scorodite and tripuhyite formed in the same $As/(As + Sb)$ ratio precursors present in the bombs prior to setting in the oven.

The total yields for the synthetic series are all below 100% (Table 3), and as the amount of Sb in the precipitates increased from $As_{100}Sb_0$ to As_0Sb_{100} the difference between measured and ideal yield increased as a function of the falling input of As and the increasing input of Sb. These low totals could be due to incomplete digestion of the precipitates and/or evaporation during the digestion process. It is well-known that As is prone to volatilization during a digestive process (Loska and Wiechuła, 2006); however, the fact that the Sb-rich members of the synthetic series were increasingly difficult to digest implies that incomplete digestion rather than volatilization was likely the principal cause. This is supported by Sb and As pre- and post-experiment concentration ratios, which show that at the Sb-rich end of the series As is enriched relative to Sb as a function of the synthesis. For the As-end of the series the position is reversed with Sb enriched relative to As, indicating that the Sb-bearing phase (tripuhyite) at this end of the series was completely digested and/or a degree of As volatilization occurred. It should, be emphasized, however, that the comparative antimony depletion shown by the Sb-rich series members was markedly greater than the arsenic depletion shown by As-rich series members (Table 3). This observation further supports the view that the most likely
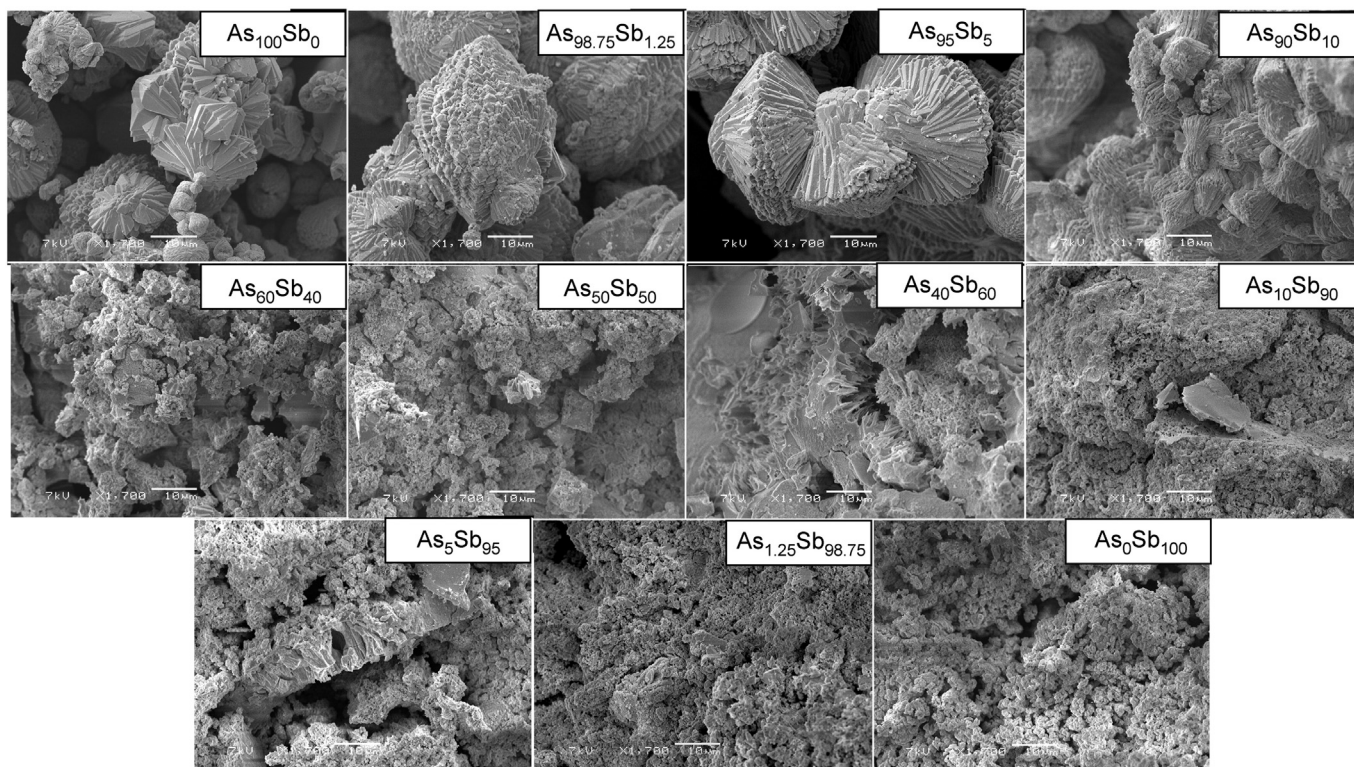
Fig. 6. SEM photomicrographs of synthetic precipitates.

explanation for the falling yield pattern is the increasing presence of a Sb-bearing phase (tripuhyite) which is resistant to digestion.

3.1.4. µXRF mapping

µXRF mapping was used to evaluate the distribution of As and Sb in the synthetic compounds, and to provide information about the types and speciation of Sb, respectively. The µXRF mapping showed that As and Sb were anti-correlated in the synthetic compounds (e.g., $As_{1.25}Sb_{98.75}$, Fig. 7).

3.2. Arsenic and Sb concentrations of natural scorodite samples

Scorodite is widespread geographically, with 967 reported locations listed on Mindat (Mindat, 2014). We analysed scorodite samples from every continent apart from Antarctica (Table 4), to determine whether the scorodites contained any Sb. The scorodite samples were blue or green, and occurred as crust-like alteration products of arsenopyrite

and löllingite, or as well-formed crystals within a host matrix or, most commonly, in isolation (Table 4; c.f., Mihaljevič et al., 2010).

Each of the 36 natural scorodite samples was analysed at least six times by EMPA. Two of the samples showed no detectable amounts of Sb (LOD = 0.005 wt.%). Others showed minimal Sb; for example the sample from Tsumeb, Namibia showed detectable Sb (0.009 wt.%) at just one of the six points used to analyse this grain. The range of concentrations shown across the individual sample points ranged from this minimum 0.009 wt.% to a maximum of 0. 615 wt.% in a sample sourced from Bradda Head, Isle of Man. The later sample also had the highest mean Sb concentration of 0. 362 wt.% Sb (n = 12). This latter sample appeared to be forming from an arsenopyrite precursor.

Table 3
Chemical digestion results for synthetic As–Sb precipitates.

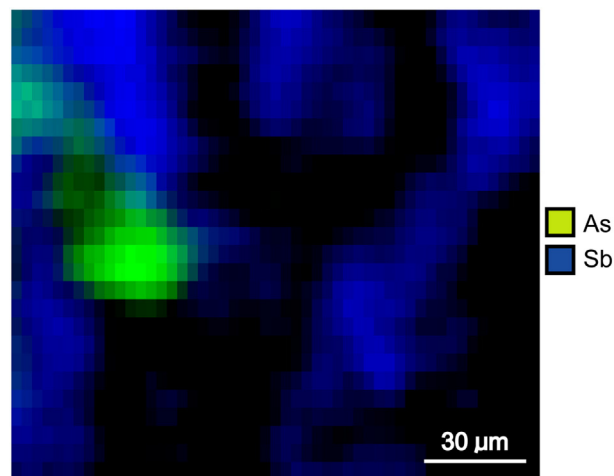| Sample	As (mol.%)	Fe (mol.%)	Sb (mol.%)	Yield (%)	Molar Sb/As	Initial Sb, As mol ratio
$As_{100}Sb_0$	0.42	0.40	0.00	97.3	0.00	–
$As_{98.75}Sb_{1.25}$	0.39	0.38	0.00	94.1	0.012	0.013
$As_{95}Sb_5$	0.35	0.36	0.02	91.6	0.059	0.026
$As_{90}Sb_{10}$	0.37	0.39	0.04	96.0	0.116	0.053
$As_{60}Sb_{40}$	0.21	0.39	0.19	97.2	0.948	0.667
$As_{50}Sb_{50}$	0.14	0.39	0.25	97.9	1.822	1.000
$As_{40}Sb_{60}$	0.10	0.37	0.29	96.4	2.856	1.500
$As_{10}Sb_{90}$	0.04	0.35	0.34	92.1	8.997	19.000
As_5Sb_{95}	0.02	0.31	0.32	85.4	15.674	39.000
$As_{1.25}Sb_{98.75}$	0.01	0.32	0.33	85.3	30.960	79.000
As_0Sb_{100}	0.00	0.29	0.29	78.8	–	–

Fig. 7. µXRF map showing distribution and anti-correlation of As and Sb in precipitate $As_{1.25}Sb_{98.75}$.

Table 4
Electron microprobe analysis of natural scorodite samples.

| Country	Location	Habit	As (wt.%)	Sb (wt.%)	Fe (wt.%)	O (wt.%)
Australia	Elsmore Sn mine, New South Wales	Isolated crystal(s)	33.92 ± 2.79	0.01 ± 0.02	35.65 ± 0.95	32.42 ± 3.36
Australia	Mt Piper, Broadford, Victoria	Scorodite weathering from arsenopyrite	32.68 ± 0.46	0.00 ± 0.01	33.37 ± 0.34	33.95 ± 3.36
Australia	Return Creek, Herberton, Queensland	Isolated crystal(s)	33.38 ± 0.55	0.01 ± 0.01	33.91 ± 0.35	32.70 ± 0.83
Brazil	Unknown	Isolated crystal(s)	33.63 ± 0.44	0.00 ± 0.00	33.94 ± 0.96	32.44 ± 0.96
Brazil	Minas Gerais	Isolated crystal(s)	38.46 ± 2.42	0.01 ± 0.02	34.24 ± 1.58	27.30 ± 3.94
China	Barshichang village, Hezhous, Guanxi	Isolated crystal(s)	30.33 ± 0.34	0.02 ± 0.02	30.65 ± 0.21	39.00 ± 0.19
China	Guangxi	Isolated crystal(s)	34.94 ± 1.46	0.02 ± 0.02	34.22 ± 0.46	30.84 ± 1.22
China	Hezhou, Guangxi	Scorodite associated with pyrite	30.39 ± 0.22	0.03 ± 0.03	32.07 ± 0.16	37.52 ± 0.09
China	Hezhou, Guangxi	Isolated crystals	30.88 ± 0.32	0.03 ± 0.03	32.07 ± 0.16	37.52 ± 0.09
China	Hezhou, Guangxi	Isolated crystals	30.98 ± 0.48	0.01 ± 0.02	33.31 ± 0.53	35.70 ± 0.17
France	Salsigne, Aude	Isolated crystal(s)	33.51 ± 0.61	0.01 ± 0.01	33.91 ± 0.50	32.57 ± 0.81
Germany	Graul, Saxony	Isolated crystal(s)	32.25 ± 0.66	0.01 ± 0.01	33.22 ± 0.38	33.52 ± 0.95
Germany	Rheinland-Pfalz, Montabaur, Gernbach	Isolated crystal(s)	38.45 ± 0.95	0.01 ± 0.01	27.25 ± 0.50	34.29 ± 1.13
Germany	Sazony, Schwarzenberg, Graul Mine	Isolated crystal(s)	36.15 ± 0.30	0.01 ± 0.01	32.94 ± 0.22	30.90 ± 1.13
Ireland	County Galway, Tynagh Mine	Isolated crystal(s)	34.28 ± 2.62	0.00 ± 0.01	32.07 ± 2.42	33.64 ± 3.86
Ireland	County Galway, Tynagh Mine	Isolated crystal(s)	31.74 ± 0.59	0.00 ± 0.00	34.82 ± 2.08	33.43 ± 2.33
Japan	Kiura Mine, Oita Prefecture	Scorodite enclosing löllingite	33.55 ± 1.09	0.01 ± 0.01	33.72 ± 1.18	32.72 ± 1.73
Mexico	Concepcion del Oro, Zacatecas	Isolated crystal(s)	33.61 ± 0.50	0.00 ± 0.01	34.02 ± 0.40	32.36 ± 0.82
Mexico	Mapimi	Isolated crystal(s)	35.01 ± 1.77	0.00 ± 0.01	34.02 ± 0.40	32.36 ± 0.82
Namibia	Tsumeb	Isolated crystals	33.32 ± 0.45	0.00 ± 0.00	30.71 ± 0.32	35.97 ± 0.31
UK	Bradda Head, Port Erin, Isle of Man	Scorodite weathering from arsenopyrite and rimming quartz	36.86 ± 1.24	0.36 ± 0.13	33.50 ± 0.98	29.28 ± 2.03
UK	Bradda Head, Port Erin, Isle of Man	Isolated crystal(s)	33.36 ± 3.76	0.01 ± 0.01	35.64 ± 1.14	29.28 ± 3.27
UK	Caldbeck Fells, Cumbria	Isolated crystal(s)	34.16 ± 1.15	0.01 ± 0.01	32.74 ± 0.67	33.09 ± 1.22
UK	Caldbeck Fells, Cumbria	Isolated crystal(s)	35.00 ± 4.45	0.00 ± 0.00	29.68 ± 2.48	35.31 ± 6.70
UK	Carrock Fell, Cumbria	Scorodite rimming quartz	31.66 ± 1.01	0.03 ± 0.02	31.47 ± 3.02	36.84 ± 2.11
UK	Causey Pike, Keswick, Cumbria	Isolated crystal(s)	33.36 ± 3.76	0.00 ± 0.00	34.36 ± 2.52	32.29 ± 2.85
UK	Danescombe Mine, Calstock, Cornwall	Isolated crystal(s)	33.20 ± 0.75	0.01 ± 0.01	32.92 ± 1.45	32.29 ± 2.09
UK	Hemerdon Mine, Plymouth, Devon	Isolated crystals	31.29 ± 0.21	0.01 ± 0.01	30.54 ± 0.18	38.16 ± 0.32
UK	Hemerdon Mine, Plymouth, Devon	Isolated crystals	33.01 ± 0.99	0.01 ± 0.01	31.67 ± 0.75	35.31 ± 0.25
UK	Hingston Quarry, Cornwall	Scorodite rimming quartz	33.68 ± 0.72	0.01 ± 0.01	25.31 ± 0.26	41.00 ± 0.97
UK	Mulberry Pit, Lanlivet, Cornwall	Isolated crystal(s)	34.91 ± 1.93	0.01 ± 0.01	31.42 ± 3.40	33.67 ± 1.61
UK	Wheal Gorland, St. Day, Cornwall	Scorodite weathering from arsenopyrite	31.94 ± 0.90	0.01 ± 0.02	27.58 ± 1.40	40.47 ± 0.82
USA	Gold Hill Mine, Toole County, Utah	Isolated crystals	32.37 ± 0.45	0.06 ± 0.05	29.51 ± 0.54	38.05 ± 0.75
USA	Gold Hill Mine, Toole County, Utah	Isolated crystals	30.76 ± 0.24	0.08 ± 0.03	31.05 ± 2.06	38.11 ± 1.96
USA	Gold Hill Mine, Toole County, Utah	Scorodite with covellite inclusions	33.15 ± 0.14	0.07 ± 0.05	33.85 ± 0.26	32.94 ± 0.28
USA	Gold Hill Mine, Toole County, Utah	Isolated crystal(s)	39.52 ± 2.25	0.05 ± 0.03	36.17 ± 1.45	24.27 ± 2.43

3.3. Behaviour of Sb in the As–Fe–Sb–O system

Our Munsell colour, XRD and μXRF mapping analysis have shown that when Sb is introduced to the As–Fe–O system via scorodite precipitation, the distinct phases scorodite and tripuhyite form. The powder XRD data suggest that there is no detectable As–Sb solid solution in scorodite. This agrees with our EPMA data for the natural samples (Table 4) that suggests that the scorodite does not incorporate significant amounts of Sb.

The synthetic scorodite produced in this study is well-crystallised, whereas tripuhyite is poorly-crystallised (Fig. 2). The morphology of the scorodite phases changes, however, from crystalline rosettes to blocky masses when between 10 and 40 M Sb/(As + Sb) is added to the synthesis solutions, and the blocky masses persist with increasing amounts of Sb (Fig. 6). The presence of impurities such as Sb is known to inhibit mineral crystallisation, as the impurities can block or retard the growth of dominant crystal faces (Wright, 2009). Moreover, the competition for common ions between minerals may cause the formation of one to be inhibited, particularly when there are differences in the kinetics of formation and the relative thermodynamic stability of the minerals (Giocondi et al., 2010).

Tripuhyite has been increasingly reported in studies of mine wastes, perhaps as a function of improving characterisation techniques (e.g., Majzlan et al., 2011; Mitsunobu et al., 2011; Leverett et al., 2012; Roper et al., 2012). Some of these authors note that the previous underestimation of the prevalence of tripuhyite may be a function of its often nano-crystalline habit (Mitsunobu et al., 2011) and its orange-red colour, leading to misidentification as Fe oxy/hydroxide (Leverett et al., 2012; Roper et al., 2012).

We have corroborated previous work reporting the high stability of tripuhyite and the conservative environmental behaviour of Sb with our chemical digestion data (Table 3) by demonstrating the relative insolubility, and therefore likely low bioaccessibility, of tripuhyite. Other authors have established that tripuhyite is an extremely stable phase, significantly more stable than scorodite or goethite (Leverett et al., 2012). After the oxidation of primary As- and Sb-bearing sulphides, fractionation between As and Sb has been reported frequently, almost always with As being significantly more mobile than Sb (e.g., Flynn et al., 2003; Tighe et al., 2005; Diemar et al., 2009; Ettler et al., 2010: Frohne et al., 2011). It might therefore be concluded that the secondary mineral hosting Sb is more stable than that of As (cf., Wilson et al., 2004). In a wider environmental context the high stability of tripuhyite may well be an important factor in explaining the conservative environmental behaviour pattern of Sb. For example, it has been proposed that iron/oxy hydroxide minerals (e.g., goethite) can readily be transformed into tripuhyite (Leverett et al., 2012), as shown below:

$$FeOOH_{(s)} + Sb(OH)_{5\,(aq)}^{\circ} = FeSbO_{4(s)} + 3H_2O_{(l)} \qquad (3)$$
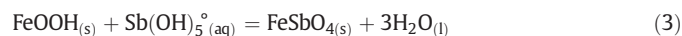
The log equilibrium constant (log K) of Eq. (3) is +11.0 (at 298.15 K). It can therefore be concluded that goethite is unstable with respect to tripuhyite even at very small (tens of parts per trillion) activities of Sb(V) in aqueous solution (Leverett et al., 2012; Bolanz et al., 2013). It should also be noted, however, that sorption of Sb to Fe oxy/hydroxide minerals is also a real, often reversible, phenomenon (McComb et al., 2007). In reality a spectrum of Sb hosting behaviour is likely to exist between the two absolute end members of surface mediated-sorption

and -nano-crystallisation; positions on this spectrum will be constrained by the pertaining mineralogical, physical and chemical circumstances. The 'Sb-scavenging' mechanism caused by tripuhyite formation likely explains the reported presence of nano-sized tripuhyite crystals reported from pegmatites (e.g., Novák et al., 2004). It has been established that both As and Sb behave as incompatible elements during magmatic processes, in the absence of sulphide in the fluid phase, and are thereby concentrated in pegmatites (e.g., Noll et al., 1996; Melcher et al., 2015). Hence, Sb is present in the final stages of melt crystallisation, where it may be scavenged, even where there is only a low concentration of Fe, to form the highly stable tripuhyite. In this context, it is also worth noting that tripuhyite was originally characterised as 'micro-crystalline aggregates' in alluvial deposits derived from the weathering of pegmatites at Tripuhy, Brazil (Hussak and Prior, 1897).

It is of interest to speculate on the origin of the markedly high stability of the tripuhyite lattice. It is well established that the two key constraints on lattice stability are the products of the total of change of the component ions and the number of ions in each formula unit (directly proportional to stability) together with the sum of the atomic radii of the participating ions (inversely proportional to stability). These relationships are semi-quantitatively described by the Kapustinskii Eq. (4) (a simplified form of the quantitative Born–Landé equation) (Gale, 1996):

$$L = \frac{WvZ+Z-}{r++r-} \qquad (4)$$

where L is the lattice energy (kJ mol^{-1}), W is a constant equal to $1.079 * 10^5$ kJ mol^{-1}, v is the number of ions in each formula unit, $Z+$ and $Z-$ are the numbers of positive and negative charges and $r+$ and $r-$ are the radii of the positive and negative ions, expressed in pm. The equation has been extended to approximate the lattice energies of crystals with multiple ions such as tripuhyite (Glasser, 1995; Glasser and Jenkins, 2000) which further refine the lattice energy's direct relationship with charge and indirect one with inter-nuclear distance/unit cell volume. Hence, the high charge of the scorodite and tripuhyite unit cells is the principal reason for these phases' high environmental stability. The interposition of the two water molecules in the scorodite framework, however, mean that despite the smaller ionic radius of As(V) (60 pm) compared to Sb(V) (74 pm), Sb-bearing tripuhyite is the more stable mineral of the pair. Indeed, the cell volume of scorodite is of the order of 927–928 Å^3 (Fig. 4), whereas Berlepsch et al. (2003) give a unit cell a dimension of c. 4.63 Å and a c dimension of c. 3.06 Å for the tetragonal phase tripuhyite. These latter dimensions compute to give the appreciably smaller tripuhyite unit cell volume of c. 66 Å^3, explaining the former phase's higher lattice energy and stability. This argument can be extended to conditions of low Eh where the Sb^{III}- and Fe^{II}-bearing mineral schafarzikite (FeSb$_2$O$_4$) is also predicted to stable on the basis of the Kapustinskii criteria (Leverett et al., 2012). In the context of a reducing (anoxic) environment it is also worth noting that schafarzikite has no reported analogous reduced As-bearing phase. Thus, in the absence of other constraining factors, the comparatively conservative behaviour of Sb compared to As at the surface can be predicted to be heightened at depth, perhaps as a function of sediment burial.

3.4. Crystal structure of scorodite and lack of Sb incorporation

In oxidized mine waste environments, As and Sb mostly both occur as oxidized species (i.e., As(V), Sb(V); e.g., Kossoff et al., 2012). Antimony is chemically similar to As, with both metalloids lying in group 15 of the Periodic Table. They possess the ground state valence configuration of $5s^2\ 4d^{10}\ 5p^3$ (Sb) and $4s^2\ 3d^{10}\ 4p^3$ (As), and, therefore, they often occur together or on occasion substitute for one another

in minerals (e.g., in the tetrahedrite to tennantite solid solution series $Cu_{12}(As,Sb)_4S_{13}$). However, Sb(V) is a larger ion than As(V) and, for steric reasons, is often octahedrally coordinated with oxygen (compare 74 pm for octahedrally coordinated Sb(V) with 47.5 pm for tetrahedrally coordinated As(V) and 60 pm for octahedrally coordinated As(V); Shannon, 1976). The larger size and different co-ordination of Sb(V) compared to As(V) suggests that substitution of the Sb(V) for the As(V) in scorodite is either unlikely or limited, and this has been shown by our co-precipitation experiments.

4. Conclusions

During precipitation of scorodite in the presence of Sb, the Sb does not substitute in scorodite, probably due to its large radius and octahedral coordination with O (compared to the tetrahedral coordination of As with O in scorodite). The introduction of increasing concentrations of Sb to the Fe–As–O system when scorodite precipitates affects the morphology of the scorodite, and results in the precipitation of the highly insoluble phase tripuhyite. Tripuhyite has a markedly high lattice energy, which likely renders it a long-term environmental sink for Sb. Its abundance has probably been previously underestimated, most likely as a result of both its Fe oxyhydroxide-like appearance and commonly reported nano–micro crystalline habit. It is therefore conceivable that a significant proportion of what has previously described as Sb sorbed to Fe oxyhydroxides is in fact distinct nano-crystalline assemblages of tripuhyite, and further work is required to test this hypothesis. The higher stability of tripuhyite relative to scorodite could be a significant factor in explaining the often observed lower environmental mobility of Sb compared to As; for example, in oxic mine waste environments. However, other relatively insoluble Sb-bearing phases such as valentinite and senarmontite (both Sb$_2$O$_3$) have been reported in mine wastes (e.g., Filella et al., 2009), and these are stable under moderately oxidizing conditions (Leverett et al., 2012), so they too are likely to play a role in explaining the low environmental mobility of Sb, particularly under conditions of comparatively low Fe activity.

References

Anawar, H.M., Freitas, M.C., Canha, N., Santa Regina, I., 2011. Arsenic, antimony, and other trace element contamination in a mine tailings affected area and uptake by tolerant plant species. Environ. Geochem. Health 33, 353–362.
Berlepsch, P., Armbruster, T., Brugger, J., Criddle, A.J., Graeser, S., 2003. Tripuhyite, FeSbO$_4$, revisited. Min. Mag. 67, 31–46.

Bolanz, R.M., Bläss, U., Ackermann, S., Ciobotă, V., Rösch, P., Tarcea, N., Popp, J., Majzlan, J., 2013. The effect of antimonate, arsenate, and phosphate on the transformation of ferrihydrite to goethite, hematite, feroxyhyte, and tripuhyite. Clays Clay Minerals 61 (1), 11–25.

Centeno, J.A., Mullick, F.G., Martinez, L., Page, N.P., Gibb, H., Longfellow, D., Thompson, C., Ladich, E.R., 2002. Pathology related to chronic arsenic exposure. Environ. Health Perspect. 110 (Suppl. 5), 883.

Cidu, R., Biddau, R., Dore, E., Vacca, A., Marini, L., 2014. Antimony in the soil–water–plant system at the Su Suergiu abandoned mine (Sardinia, Italy): strategies to mitigate contamination. Sci. Total Environ. 497–498, 319–331.

Cummings, D.E., Caccavo, F., Fendorf, S., Rosenzweig, R.F., 1999. Arsenic mobilization by the dissimilatory Fe (III)-reducing bacterium *Shewanella alga* BrY. Environ. Sci. Technol. 33, 723–729.

Diemar, G.A., Filella, M., Leverett, P., Williams, P.A., 2009. Dispersion of antimony from oxidizing ore deposits. Pure Appl. Chem. 81, 1547–1553.

Drahota, P., Filippi, M., 2009. Secondary arsenic minerals in the environment: a review. Environ. Int. 35, 1243–1255.

Ettler, V., Tejneck, V., Mihaljevič, M., Šebek, O., Zuna, M., Vaněk, A., 2010. Antimony mobility in lead smelter-polluted soils. Geoderma 155, 409–418.

Filella, M., Belzile, N., Chen, Y.-W., 2002. Antimony in the environment: a review focused on natural waters: I. Occurrence. Earth-Sci. Rev. 57, 125–176.

Filella, M., Philippo, S., Belzile, N., Chen, Y., Quentel, F., 2009. Natural attenuation processes applying to antimony: a study in the abandoned antimony mine in Goesdorft, Lexembourg. Sci. Total Environ. 407, 6205–6216.

Flynn, H.C., Meharg, A.A., Bowyer, P.K., Paton, G.I., 2003. Antimony bioavailability in mine soils. Environ. Pollut. 124, 93–100.

Friedl, J., Wagner, F.E., Sawicki, J.A., Harris, D.C., Mandarino, J.A., Marion, P., 1992. ^{197}Au, ^{57}Fe and ^{121}Sb Mössbauer study of gold minerals and ores. Hyperfine Interact. 70, 945–948.

Frohne, T., Rinklebe, J., Diaz-Bone, R.A., Du Laing, G., 2011. Controlled variation of redox conditions in a floodplain soil: impact on metal mobilization and biomethylation of arsenic and antimony. Geoderma 160, 414–424.

Fu, Z., Wu, F., Amarasiriwardena, D., Mo, C., Liu, B., Zhu, J., Deng, Q., Liao, H., 2010. Antimony, arsenic and mercury in the aquatic environment and fish in a large antimony mining area in Hunan, China. Sci. Total Environ. 408, 3403–3410.

Gale, J.D., 1996. Empirical potential derivation for ionic materials. Phil. Mag. B 73, 3–19.

Gill, R., 1997. Modern Analytical Geochemistry. Longman, Harlow, Essex, England.

Giocondi, J.L., El-Dasher, B., Nancollas, G.H., Orme, C.A., 2010. Molecular mechanisms of crystallization impacting calcium phosphate cements. Phil. Trans. R. Soc. A 368, 1937–1961.

Glasser, L., 1995. Lattice energies of crystals with multiple ions: a generalized Kapustinskii equation. Inorg. Chem. 34, 4935–4936.

Glasser, L., Jenkins, H.D.B., 2000. Lattice energies and unit cell volumes of complex ionic solids. J. Am. Chem. Soc. 122, 632–638.

Gonzalez-Contreras, P., Weijma, J., Van der Wiejden, R., Buisman, C.J.N., 2010. Biogenic scorodite crystallization by *Acidianus sulfidivorans* for arsenic removal. Environ. Sci. Technol. 44, 675–680.

Gordon, R.B., Bertram, M., Graedel, T.E., 2006. Metal stocks and sustainability. Proc. Natl. Acad. Sci. U. S. A. 103, 1209–1214.

Grau-Crespo, R., de Leeuw, N.H., Catlow, C.R.A., 2004. Distribution of cations in FeSbO₄: a computer modeling study. Chem. Mater. 16, 1954–1960.

Haffert, L., Craw, D., 2008. Mineralogical controls on environmental mobility of arsenic from historic mine processing residues, New Zealand. Appl. Geochem. 23, 1467–1483.

Hussak, E., Prior, G.T., 1897. On tripuhyite, a new antimonate of iron, from Tripuhy, Brazil. Min. Mag. 11, 302–303.

Jia, Y., Xu, L., Fang, Z., Demopoulos, G.P., 2006. Observation of surface precipitation of arsenate on ferrihydrite. Environ. Sci. Technol. 40, 3248–3253.

Kossoff, D., Hudson-Edwards, K.A., Dubbin, W.E., Alfredsson, M., Geraki, T., 2012. Cycling of As, P, Pb and Sb during weathering of mine tailings: implications for fluvial environments. Min. Mag. 76, 1209–1228.

Lalinská-Voleková, B., Majzlan, J., Klimko, T., Chovan, M., Kučerová, G., Michňová, J., Steininger, R., 2012. Mineralogy of weathering products of Fe–As–Sb mine wastes and soils at several Sb deposits in Slovakia. Can. Mineral. 50, 481–500.

Larson, A.C., Von Dreele, R.B., 2004. General structure analysis system (GSAS). Los Alamos National Laboratory Report LAUR 86-748.

Le Berre, J.F., Gauvin, R., Demopoulos, G.P., 2008. A study of the crystallization kinetics of scorodite via the transformation of poorly crystalline ferric arsenate in weakly acidic solution. Colloids Surf. A 315, 117–129.

Leverett, P., Reynolds, J.K., Roper, A.J., Williams, P.A., 2012. Tripuhyite and schafarzikite: two of the ultimate sinks for antimony in the natural environment. Min. Mag. 76, 891–902.

Loska, K., Wiechuła, D., 2006. Comparison of sample digestion procedures for the determination of arsenic in bottom sediment using hydride generation AAS. Microchim. Acta 154, 235–240.

Maiti, S., Chattopadhyay, S., Deb, B., Samanta, T., Maji, G., Pan, B., Ghosh, A., Ghosh, D., 2012. Antioxidant and metabolic impairment result in DNA damage in arsenic-exposed individuals with severe dermatological manifestations in Eastern India. Environ. Toxicol. 27, 342–350.

Majzlan, J., Lalinská, B., Chovan, M., Jurkovič, L., Milovská, S., Göttlicher, J., 2007. The formation, structure, and ageing of As-rich hydrous ferric oxide at the abandoned Sb deposit Pezinok (Slovakia). Geochim. Cosmochim. Acta 71, 4206–4220.

Majzlan, J., Lalinská, B., Chovan, M., Bläß, U., Brecht, B., Göttlicher, J., Steininger, R., Hug, K., Zeigler, S., Gescher, J., 2011. A mineralogical, geochemical, and microbiological assessment of the antimony- and arsenic-rich neutral mine drainage tailings near Pezinok, Slovakia. Am. Mineral. 96, 1–13.

Majzlan, J., Drahota, P., Filippi, M., Grevel, K.-D., Kahl, W.-A., Plášil, J., Boerio-Goates, J., Woodfield, B.F., 2012. Thermodynamic properties of scorodite and parascorodite (FeAsO₄·2H₂O), kaňkite (FeAsO₄·3.5H₂O), and FeAsO₄. Hydrometall. 117–118, 47–56.

McComb, K.A., Craw, D., McQuillan, A.J., 2007. ATR-IR spectroscopic study of antimonate adsorption to iron oxide. Langmuir 23, 12125–12130.

Melcher, F., Graupner, T., Gäbler, H.E., Sitnikova, M., Henjes-Kunst, F., Oberthür, T., Gerdes, A., Dewaele, S., 2015. Tantalum–(niobium–tin) mineralisation in African pegmatites and rare metal granites: constraints from Ta–Nb oxide mineralogy, geochemistry and U–Pb geochronology. Ore Geol. Rev. 64, 667–719.

Meunier, L., Walker, S.R., Wragg, J., Parsons, M.B., Koch, I., Jamieson, H.E., Reimer, K.J., 2010. Effects of soil composition and mineralogy on the bioaccessibility of arsenic from tailings and soil in gold mine districts of Nova Scotia. Environ. Sci. Technol. 44, 2667–2674.

Mihaljevič, M., Ettler, V., Šebek, O., Drahota, P., Strnad, L., Procházka, R., Zeman, J, Sracek, O., 2010. Alteration of arsenopyrite in soils under different vegetation covers. Sci. Total Environ. 408, 1286–1294.

Mindat, 2014. http://www.mindat.org/ (Accessed 14/02/2014//).

Mitsunobu, S., Takahashi, Y., Utsunomiya, S., Marcus, M.A., Terada, Y., Iwamura, T., Sakata, M., 2011. Identification and characterization of nanosized tripuhyite in soil near Sb mine tailings. Am. Mineral. 96, 1171–1181.

Mudd, G.M., 2010. The environmental sustainability of mining in Australia: key mega-trends and looming constraints. Resour. Policy 35, 98–115.

Noll Jr., P.D., Newsom, H.E., Leeman, W.P., Ryan, J.G., 1996. The role of hydrothermal fluids in the production of subduction zone magmas: evidence from siderophile and chalcophile trace elements and boron. Geochim. Cosmochim. Acta 60, 587–611.

Nordstrom, D.K., Majzlan, J., Königsberger, E., 2014. Thermodynamic properties for arsenic minerals and aqueous species. Rev. Mineral. Geochem. 79, 217–255.

Novák, M., Černý, P., Cempírek, J., Šrein, V., Filip, J., 2004. Ferrotapiolite as a pseudomorph of stibiotantalite from the Laštovičky lepidolite pegmatite, Czech Republic; an example of hydrothermal alteration at constant Ta/(Ta + Nb). Can. Mineral. 42, 1117–1128.

Paktunc, D., Bruggeman, K., 2010. Solubility of nanocrystalline scorodite and amorphous ferric arsenate: implications for stabilization of arsenic in mine wastes. Appl. Geochem. 25, 674–683.

Paktunc, D., Dutrizac, J., Gersman, V., 2008. Synthesis and phase transformations involving scorodite, ferric arsenate and arsenical ferrihydrite: implications for arsenic mobility. Geochim. Cosmochim. Acta 72, 2649–2672.

Pershagen, G., Bergman, F., Klominek, J., Damber, L., Wall, S., 1987. Histological types of lung cancer among smelter workers exposed to arsenic. Br. J. Ind. Med. 44, 454–458.

Recio-Vazquez, L., Garcia-Guinea, J., Carral, P., Alvarez, A.M., Garrido, F., 2011. Arsenic mining waste in the catchment area of the Madrid detrital aquifer (Spain). Water Air Soil Pollut. 214, 307–320.

Roper, A.J., Williams, P.A., Filella, M., 2012. Secondary antimony minerals: phases that control the dispersion of antimony in the supergene zone. Chem. Erde-Geochem. 72, 9–14.

Salzsauler, K.A., Sidenko, N.V., Sherriff, B.L., 2005. Arsenic mobility in alteration products of sulfide-rich, arsenopyrite-bearing mine wastes, Snow Lake, Manitoba, Canada. Appl. Geochem. 20, 2303–2314.

Savage, K.S., Tingle, T.N., O'Day, P.A., Waychunas, G.A., Bird, D.K., 2000. Arsenic speciation in pyrite and secondary weathering phases, Mother Lode Gold District, Tuolumne County, California. Appl. Geochem. 15, 1219–1244.

Savage, K.S., Bird, D.K., O'Day, P.A., 2005. Arsenic speciation in synthetic jarosite. Chem. Geol. 215, 473–498.

Shannon, R.D., 1976. Revised effective ionic radii and systematic studies of interatomic distances in halides and chalcogenides. Acta Crystallogr. A32, 751–767.

Smedley, P.L., Kinniburgh, D.G., 2002. A review of the source, behaviour and distribution of arsenic in natural waters. Appl. Geochem. 17, 517–568.

States, J.C., Barchowsky, A., Cartwright, I.L., Reichard, J.F., Futscher, B.W., Lantz, R.C., 2011. Arsenic toxicology: translating between experimental models and human pathology. Environ. Health Perspect. 119, 1356.

Tighe, M., Ashley, P., Lockwood, P., Wilson, S., 2005. Soil, water, and pasture enrichment of antimony and arsenic within a coastal floodplain system. Sci. Total Environ. 347, 175–186.

Wilson, N.J., Craw, D., Hunter, K., 2004. Antimony distribution and environmental mobility at an historic antimony smelter site, New Zealand. Environ. Pollut. 129, 257–266.

Wright, K.V., 2009. The incorporation of cadmium, manganese and ferrous iron in sphalerite: insights from computer simulations. Can. Mineral. 47, 615–623.

Wu, F., Fu, Z., Liu, B., Mo, C., Chen, B., Corns, W., Liao, H., 2011. Health risk associated with dietary co-exposure to high levels of antimony and arsenic in the world's largest antimony mine area. Sci. Total Environ. 409, 3344–3351.

Xu, Y., Zhou, G.P., Zheng, X.F., 2007. Redetermination of iron(III) arsenate dihydrate. Acta Crystallogr. E63, i67–i69.

Yáñez, L., García-Nieto, E., Rojas, E., Carrizales, L., Mejía, J., Calderón, J., Razo, I., Díaz-Barriga, F., 2003. DNA damage in blood cells from children exposed to arsenic and lead in a mining area. Environ. Res. 93, 231–240.